Turbulent Upper-Ocean Mixing Affected by Meltwater Layers during Arctic Summer

Achim Randelhoff

Institute for Arctic and Marine Biology, University of Tromsø, The Arctic University of Norway, and Norwegian Polar Institute, Tromsø, Norway

Ilker Fer

Geophysical Institute, University of Bergen, and Bjerknes Centre for Climate Research, Bergen, Norway

Arild Sundfjord

Norwegian Polar Institute, Tromsø, Norway

(Manuscript received 30 August 2016, in final form 30 January 2017)

ABSTRACT

Every summer, intense sea ice melt around the margins of the Arctic pack ice leads to a stratified surface layer, potentially without a traditional surface mixed layer. The associated strengthening of near-surface stratification has important consequences for the redistribution of near-inertial energy, ice–ocean heat fluxes, and vertical replenishment of nutrients required for biological growth. The authors describe the vertical structure of meltwater layers and quantify their seasonal evolution and their effect on turbulent mixing in the oceanic boundary layer by analyzing more than 450 vertical profiles of velocity microstructure in the seasonal ice zone north of Svalbard. The vertical structure of the density profiles can be summarized by an equivalent mixed layer depth h_{BD}, which scales with the depth of the seasonal stratification. As the season progresses and melt rates increase, h_{BD} shoals following a robust pattern, implying stronger vertical stratification, weaker vertical eddy diffusivity, and reduced vertical extent of the mixing layer, which is bounded by h_{BD}. Through most of the seasonal pycnocline, the vertical eddy diffusivity scales inversely with buoyancy frequency ($K_\rho \propto N^{-1}$). The presence of mobile sea ice alters the magnitude and vertical structure of turbulent mixing primarily through stronger and shallower stratification, and thus vertical eddy diffusivity is greatly reduced under sea ice. This study uses these results to develop a quantitative model of surface layer turbulent mixing during Arctic summer and discuss the impacts of a changing sea ice cover.

1. Introduction

Stratification, currents, turbulence levels, and vertical mixing in the upper Arctic Ocean are coupled to and affected by the presence of sea ice. The sea ice cover can act like a lid to prevent input of energy from the atmosphere (Levine et al. 1985; Morison et al. 1985) and enhance or reduce the near-surface mixing (Martin et al. 2014) by changing the air–ice drag. During summer, when broken-up floes drift relatively freely, sea ice melt increases stratification as this freshwater accumulates in the upper tens of meters of the water column (Proshutinsky et al. 2009; Peralta-Ferriz and Woodgate 2015). In these conditions, the classic definition of a surface mixed layer overlying a distinct pycnocline is not necessarily applicable. Instead, the upper water column down to several tens of meters is stratified and becomes part of the seasonal pycnocline (McPhee et al. 1987; Randelhoff et al. 2014). We refer to this phenomenon as *meltwater layer* or *freshwater layer*. The meltwater layer can include, but should not be confused with, the thin, isolated freshwater lenses caught between underice ridges. In this study, we are interested in how the freshwater layer shapes the seasonal pycnocline. It is of secondary importance whether or not there is a mixed layer in the classical sense, as long as it is shallow relative to the extent of the seasonal pycnocline.

The marginal ice zone (MIZ) between the interior pack ice and the open ocean is characterized by low ice

Corresponding author e-mail: Achim Randelhoff, achim@npolar.no

DOI: 10.1175/JPO-D-16-0200.1

concentrations, high melt rates, and strong horizontal gradients. Spatial variability in ice conditions, melt rates, and turbulent mixing can set up lateral density gradients over rather short distances (Timmermans and Winsor 2013). Advection and horizontal stirring might therefore also play a role in the evolution of freshwater layers.

In winter, brine rejection and intense vertical winter mixing can homogenize the upper ocean and lead to deep mixed layers before the onset of melt. This is particularly true in the weakly stratified Atlantic sector (Rudels 2016). While some remnant of previous meltwater stratification may be present in the Pacific sector, data from the Atlantic sector are characterized by vertical homogenization of the upper ocean by the end of winter.

Climate models predict both decreased summer sea ice extent in the Arctic and increased summer melt rates (Stroeve et al. 2012), leading to stronger stratification. This might increase the heat retained in the ocean and therefore shift the partitioning between solar heat directly contributing to ice melt and heat penetrating the ice cover and warming the water column (e.g., Hudson et al. 2013; Granskog et al. 2015). Furthermore, the predicted acceleration of the hydrological cycle and decadal changes in wind-driven circulation leads to a changing freshwater content of the upper Arctic Ocean (e.g., Morison et al. 2012; Haine et al. 2015). A recurrent theme also in the discussion of the fate of Arctic Ocean ecosystems is Arctic freshening, which is hypothesized to affect primary production and ecosystem composition (e.g., Li et al. 2009). We thus differentiate between two modes of freshening: a climatic one due to changes in the hydrological cycle, which freshens the polar mixed layer, and a seasonal one due to sea ice melt, which increases stratification in the turbulent ice–ocean boundary layer. It is the latter of these two modes that this study is concerned with.

Meltwater layers affect turbulent mixing in the upper ocean in multiple ways. The upper turbulent boundary layer can act as a sink for energy delivered from wind; the fraction of the energy that is not dissipated in the boundary layer is redistributed or radiated to deeper parts of the water column. Thus, meltwater layers may play an important role in altering the downward-propagating, near-inertial energy (Morison et al. 1985). When mixed layer stratification is sufficiently shallow, it can interact with sea ice drift to generate additional ice–ocean drag mediated by internal waves (McPhee and Kantha 1989).

Turbulence levels in the water column are typically gauged by the dissipation rate ε of turbulent kinetic energy, which can be directly measured by, for example, microstructure profilers. Quantification of the dissipation rate, either by observations or through its scaling and parameterization using external forcing parameters is crucial to describe the evolution of hydrography, currents, and turbulent fluxes of heat, salinity, nutrients, and momentum in the water column. The sensitivity of the overall energy budget in the upper Arctic water column to stratification and the freshwater content is still unknown.

While the research community working in the polar regions certainly is aware of the significance of these meltwater layers, we have found that their vertical structure and effect on turbulent mixing have received little attention, possibly related to the scarcity of direct turbulence observations in this environment. In this study, we present a detailed analysis of a large number of direct observations of hydrography and turbulent microstructure in the upper ocean of the MIZ during Arctic summer.

We aim to characterize the vertical distribution of meltwater in the ice–ocean boundary layer (IOBL) and how this affects the turbulent mixing in the upper ocean by setting up a predictive framework. To this end, we formulate three objectives: 1) Develop a framework to describe the hydrography and vertical structure of freshwater layers within the seasonal pycnocline by identifying key variables and how they relate to each other, 2) describe the temporal evolution of key variables on seasonal and subseasonal (e.g., weekly) time scales, and 3) quantify how these key variables relate to turbulent mixing. Each of these three objectives will be treated in their own sections. Concepts and salient explanations describing the vertical stratification and turbulence interactions exist. We aim to advance this knowledge by contributing toward a predictive understanding. Synthesizing objectives 1 to 3, we develop a quantitative model of upper-ocean mixing during the Arctic summer and how it might change in a future climate.

2. Data

a. *Datasets*

The field data used in this study were collected during four campaigns, all of them in the area around Fram Strait, the Yermak Plateau, and the Nansen Basin (Fig. 1) in the seasonal ice zone (SIZ) and the MIZ. The SIZ is defined as the region between maximum and minimum sea ice extent in late winter and late summer, respectively. The MIZ is the transition region from pack ice to open water. Two cruises of the Carbonbridge project (May and August 2014) were conducted in the MIZ. Data were sampled on these cruises in a broken-up

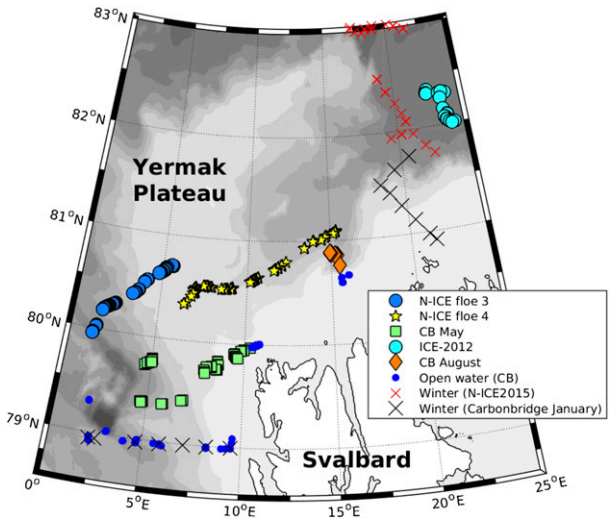

FIG. 1. Map of the study area. Profiles in open water [all from Carbonbridge (CB)] and with a deep mixed layer [winter (N-ICE2015), all ice covered; winter (Carbonbridge, January), all open water] are marked separately; all other profiles were located under varying concentrations of sea ice (see section 2a; also Table 1). Contour shading shows depths at 500-m intervals.

ice cover with small, rough ice floes (concentrations 25%–90%) and open water, as is typical of the MIZ. The other two campaigns included longer stations drifting with ice floes in a near-100% ice cover. The Norwegian Young Sea Ice Cruise (N-ICE2015) drift stations lasted from January through June 2015 (Granskog et al. 2016), including a total of four different ice floes. For this study, the focus is on the N-ICE2015 profiles measured after 25 May 2015, when upper-ocean turbulence was affected by sea ice meltwater, that is, from floe 3 (lasting until 6 June) and floe 4 (6–18 June). For N-ICE2015, the ice concentration was only occasionally as low as 85% (toward the ends of floes 3 and 4). The other ice drift camp included in this study is the 1-week ICE-2012 drift station in late July 2012 [for a description of the ice–ocean interaction, see Randelhoff et al. (2014); see also Hudson et al. (2013)].

In all campaigns, we used the MSS-90L dropsonde (IWS Wassermesstechnik) with two airfoil shear probes to measure turbulent microstructure along with temperature and conductivity in the upper 100–300 m. Note that while the conductivity sensors were regularly calibrated by the manufacturer, no calibration was performed using field data from bottle samples or other conductivity profiles. Profiles of salinity and accordingly density may therefore exhibit slight (depth independent) offsets between individual campaigns. However, as will be shown later, these potential offsets have no bearing on the quantities derived from single density profiles as all are referenced to a fixed-depth interval.

In total, we use 368 microstructure profiles sampled under ice-covered conditions that exhibit a discernible amount of meltwater as defined by the density difference between surface and a deeper level (the precise definition is given in section 3a). These are contrasted with 80 microstructure profiles sampled in open water, similarly exhibiting surface accumulation of meltwater, and 71 profiles sampled during the N-ICE2015 campaign in January and February in the Nansen Basin, when a deep (>60 m) winter mixed layer prevailed. These open-water and winter profiles are only used where explicitly stated. In addition, in order to compare the summer and winter hydrographies also in the shelf slope area, we include 15 conductivity–temperature–depth (CTD) profiles from a Carbonbridge cruise in January 2014, but note that no microstructure sampling was conducted on that cruise. See Table 1 for a detailed list of the datasets and how they were used.

During the N-ICE2015 and ICE-2012 drift stations, the vessel was moored to an ice floe, and the MSS was generally deployed several 100 m from the ship. The

TABLE 1. Dataset overview. The profile count does not include profiles not discernibly affected by meltwater (i.e., $\Delta\sigma_\theta > 0.02\ \mathrm{kg\ m^{-3}}$, see section 3a). The number of profiles is given as (under ice, in open water).

Campaign/dataset	Time	Measurement (no. of profiles)	Hydrological conditions and ice	Used for
Carbonbridge (2014)				
	January	CTD (0, 15)	Deep mixed layer, open water	Fig. 2a; illustration
	May	MSS (87, 8)	Freshwater layer, ice and open water	Main dataset
	August	MSS (39, 72)	Freshwater layer, ice and open water	Main dataset
N-ICE2015				
Winter	January–March	MSS (71, 0)	Deep mixed layer, ice	Wind speed vs mixing; Fig. 8a
Summer	June	MSS (196, 0)	Freshwater layer, ice	Main dataset
ICE-2012	July 2012	MSS (46, 0)	Freshwater layer, ice	Main dataset

Carbonbridge cruises were vessel based with frequent 24-h process stations, which permitted sampling from ice floes 100–200 m from the ship. Note that open-water stations and some ice-covered transect stations were only sampled from the vessel (all during Carbonbridge), which limited data resolution and quality, especially of turbulent microstructure, in the upper ~10–15 m of the water column.

b. MSS data processing

MSS data were processed following Fer (2006). Assuming local, small-scale isotropy (Yamazaki and Osborn 1990), dissipation of turbulent kinetic energy was estimated from the measured microscale shear as $\varepsilon = 7.5\nu\langle(\partial_z u')^2\rangle$, where ν is the molecular viscosity of seawater and $\partial_z u'$ is the turbulent shear. In practice, the portion of the shear wavenumber spectrum unaffected by high-frequency noise is integrated, and the unresolved variance is accounted for by using an empirical spectrum. Eddy diffusivity of mass is estimated from a balance struck between the shear production, buoyancy flux, and the dissipation rate and assuming a constant mixing efficiency factor corresponding to $\Gamma = 0.2$ (see section 5a), using $K_\rho = 0.2(\varepsilon/N^2)$ (Osborn 1980). The buoyancy frequency N is calculated as $N^2 = \partial b/\partial z$ with the buoyancy $b = -(g/\rho)\sigma_\theta$, where g is the gravitational acceleration, ρ is the potential density of seawater, and σ_θ is the potential density anomaly of seawater ($\sigma_\theta = \rho - 1000\,\mathrm{kg\,m^{-3}}$). The Osborn model cannot be used in well-mixed layers where $N^2 \approx 0$; however, our dataset is characterized by significant stratification (above the measurement noise level) in the entire sampled water column, including the surface layer.

c. Wind speed and wind work

Wind speed U_w is measured at 10 m from on-ice weather masts or at 24 m from the respective ship's weather mast and adjusted to 10 m as described below. To (i) make our work applicable to different ice types or even open water and (ii) give a sense of the energy transfers involved, we phrase the analysis in terms of the wind work as opposed to wind speed or ice–ocean interface stress.

Following Dewey and Moum (1990), wind work at 10 m is defined as the dot product of wind velocity and (directional) wind stress: $E_{10} = \mathbf{U}_w \cdot \tau \propto C_a\rho_a U_w^3$, where C_a is the 10-m air–ice drag coefficient, and ρ_a is the density of air. The input of turbulent energy into the ocean through the surface is then defined as $E_0 = \rho u_*^3 = (C_a\rho_a/\rho)^{1/2}E_{10}$ (following Denman and Miyake 1973), about 0.15% of E_{10}.

The value of C_a varies with type of ice cover, ice concentration, and floe size (Anderson 1987; Guest and Davidson 1987). For N-ICE2015 and ICE-2012, which took place in a similar floe size distribution, we use a value of $\approx 2.1 \times 10^{-3}$ (determined from average 10-m wind speed and air–ice momentum flux during the summer period of N-ICE2015), and for Carbonbridge, which took place closer to the ice edge and with a larger fraction of smaller floes and open water, we use $C_a = 4 \times 10^{-3}$ based on the characterization of the $2.1–5.3\times 10^{-3}$ range given by Anderson (1987) and Guest and Davidson (1987) for the MIZ.

We used the law of the wall to adjust wind speed observations at the respective vessel's wind sensors (approximately 24 m height) to 10 m following the formula $U_{10} = U_{24}\{[\log(10\,\mathrm{m}/z_0)]/[\log(24\,\mathrm{m}/z_0)]\}$, where the roughness length z_0 can be calculated from the 10-m drag coefficient as $z_0 = \exp(-0.4/\sqrt{C_a}) \times 10\,\mathrm{m}$.

d. Near-inertial energy in the upper ocean

Upper-ocean, near-inertial energy was determined for the N-ICE2015 drift campaign using complex demodulation from GPS fixes of R/V *Lance*. Underice currents were analyzed in a similar fashion, and approximate agreement between the semidiurnal clockwise components were found, indicating that ice drift and upper-ocean currents were tightly coupled. The amplitude of the clockwise, semidiurnal component of ice drift velocity was therefore computed as a measure of the strength of near-inertial oscillations in the upper ocean.

e. Melt rates and surface buoyancy fluxes

For N-ICE2015, the overall surface buoyancy flux $\langle w'b'\rangle_0$ was estimated from ice mass balance buoys in the period until 6 June 2015 (Itkin et al. 2015) and from hotwire arrays after that when a new ice floe was occupied (see A. Rösel et al. 2017, manuscript submitted to *J. Geophys. Res.*). For ICE-2012, we used $\langle w'b'\rangle_0$ as calculated by Randelhoff et al. (2014) based on measurements of the turbulent ice–ocean flux and validated by comparison with ice mass balance. For Carbonbridge, no such data are available. Stipulating an ice salinity of around 5, we converted the melt rate $\dot{h}$ ($\mathrm{cm\,day^{-1}}$) into the surface buoyancy flux by $\langle w'b'\rangle_0 = \dot{h} \times 2.4 \times 10^{-8}$ $\mathrm{W\,day\,kg^{-1}\,cm^{-1}}$, where the numerical factor is the product of ice–ocean salinity difference, ratio of ice and ocean densities, gravitational acceleration, haline contraction coefficient of seawater, and the centimeter–meter and day–second conversion factors.

3. Objective 1: A framework for the hydrography of meltwater layers in the oceanic turbulent boundary layer

In the following, we present a framework to efficiently describe types of meltwater layers. This involves identification of key variables, their relations to each other, and methods to reconstruct the full density profile from them. Campaign-averaged density profiles show the

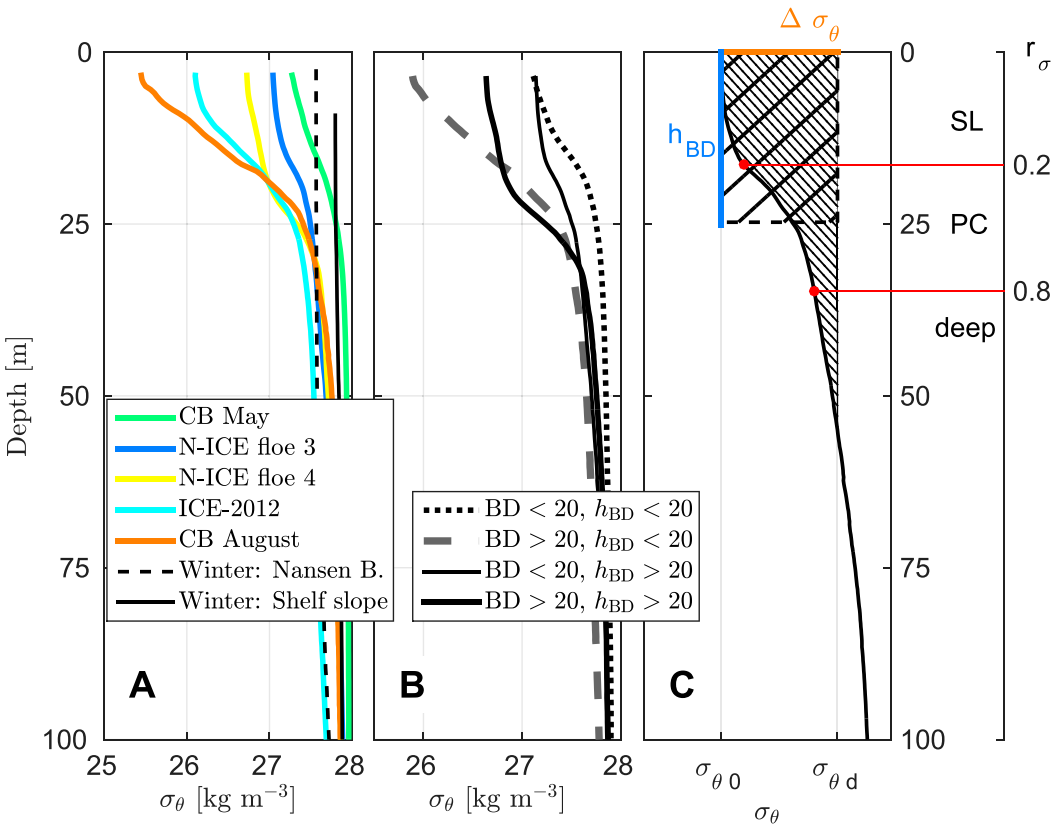

FIG. 2. (a) Survey-averaged density profiles binned by campaign or (b) by their associated buoyancy deficit BD (m) and the equivalent mixed layer depth h_{BD} (kg m^{-2}). Additionally in (a), there are winter profiles from the Nansen Basin (N-ICE2015) and from the shelf slope (Carbonbridge, January cruise). (c) Example profile illustrating the surface density deviation $\Delta\sigma_\theta$ (horizontal, orange bar), h_{BD} (vertical, blue bar), and BD (equal to each of the hatched areas). The axis on the far right gives the r_σ coordinate associated with (c) and the delineation into SL, PC, and deep layer (for definitions, see section 3a). Note the significant vertical stratification in SL.

seasonal progression from May (Carbonbridge) through June (N-ICE2015), July (ICE-2012), and August (also Carbonbridge; Fig. 2a).

a. Vertical structure

The typical summer hydrographic conditions in the seasonal ice zone do not show a surface mixed layer overlying a well-defined pycnocline. Instead, the entire upper tens of meters of the water column become seasonally stratified. It is therefore crucial to distinguish between definitions that describe various portions of the upper ocean. The surface mixed layer is classically defined as that part of the upper ocean that is well mixed with respect to physical tracers such as salinity or temperature. It is often delineated by a critical density, where the bottom of the mixed layer is defined as the shallowest depth at which density exceeds a critical density difference, relative to the surface density. Most of the profiles included in our study do not have such a surface mixed layer. Some of them might; but in order to find a framework that suits all of the profiles, we will define three regions that encompass the combined surface mixed layer (if there is one) and the seasonal pycnocline. Instead of the surface mixed layer, we define a surface layer (see below). In profiles comprising a well-mixed layer above a distinct pycnocline, the surface layer is equivalent to the surface mixed layer but not in general. The surface layer is not to be confused with the entire seasonal pycnocline or the ice–ocean (turbulent) boundary layer. The latter is that part of the upper ocean where the turbulent flow is significantly affected by the shear-driven mixing that the relative motion of ice floes and water generates.

We will employ an instrumental definition of the terms surface layer, pycnocline, and deep water column, where the three are delineated depending on their upper density relative to a deep reference density. The upper density $\sigma_{\theta 0}$ is defined as the average σ_θ over the interval 3–5 m. Based on the visual inspection of all collected density profiles, we stipulate that density stratification is well within background values by approximately 50-m

depth (Figs. 2a,b). Accordingly, we define the deep density $\sigma_{\theta d}$ as the average over the interval 45–55 m. Their difference defines the surface density deviation $\Delta\sigma_\theta = \sigma_{\theta d} - \sigma_{\theta 0}$. A profile is categorized as discernibly affected by meltwater if $\Delta\sigma_\theta > 0.02\,\mathrm{kg\,m^{-3}}$. The choice of the reference depth 45–55 m is ad hoc. However, our results are not particularly sensitive to this choice; a 10-m-deeper reference depth results in an average increase of $\Delta\sigma_\theta$ by only $0.04\,\mathrm{kg\,m^{-3}}$ and an increase of the buoyancy deficit (BD; defined below) by $2\,\mathrm{kg\,m^{-2}}$. Our choice of reference depth is motivated by a level located in a region of weak stratification, well below the depth range that is immediately affected by seasonal accumulation of meltwater. The results will then be robust against the arbitrary choice of the reference depth.

Based on these notions, we define a scaled depth coordinate $r_\sigma(z) = [\sigma_\theta(z) - \sigma_{\theta 0}]/\Delta\sigma_\theta$, which runs from 0 to 1 (values exceeding this interval are set to 0 or 1, respectively). The surface layer (SL) is defined as the depth range where $0 \le r_\sigma < 0.2$, the pycnocline (PC) is defined as the depth range where $0.2 \le r_\sigma \le 0.8$, and the deep water column comprises $0.8 < r_\sigma$ and deeper. The upper and lower extents of the PC thus correspond to the depths where the density crosses 20% and 80% of the density difference $\Delta\sigma_\theta$ between the upper and deep reference depths, respectively. In this study, the terms SL, PC, and deep follow this definition, except where stated otherwise. It has previously been demonstrated that shear in the turbulent boundary layer is mostly located in the shallow seasonal pycnocline (e.g., Randelhoff et al. 2014), such that the interval $r_\sigma = [0, 1]$ meaningfully covers the depth range where the transition between the turbulent regimes (ice–ocean interface and underlying ocean) takes place. The choices $r_\sigma = 0.2$, 0.8 are ad hoc; however, $r_\sigma = 0.2$ as the boundary between SL and PC will be justified posthoc (in our treatment of objective 3) as the boundary between where dissipation is dominated by wind versus background stratification. The choice of $r_\sigma = 0.8$ can be changed within $\pm\sim 0.1$ without any significant effect on the analysis, but this distinction is not crucial for us. It is important, however, that the PC encompasses the depth range where we expect the transition between ice drift (shear)–driven turbulence and predominantly internal wave–driven turbulence to happen.

b. Interpreting density profiles using key variables

We define the buoyancy deficit (BD) as $\int_{0\,\mathrm{m}}^{50\,\mathrm{m}} dz[\sigma_{\theta d} - \sigma_\theta(z)]$. It combines the effect of surface freshening and warming, but because of low temperatures and accordingly weak thermal expansion, and large fractions of freshwater, it is almost proportional to the freshwater content $\int dz[S_d - S(z)]$, where S_d is the deep salinity defined analogously to $\sigma_{\theta d}$. An equivalent mixed layer depth is defined as $h_{\mathrm{BD}} = \mathrm{BD}/\Delta\sigma_\theta$. Whenever the SL is well mixed and the pycnocline is sufficiently sharp, h_{BD} corresponds to the mixed layer depth in the classical sense. When h_{BD} is larger, more of the freshwater is accumulated in the SL as opposed to the PC, relatively speaking. The term h_{BD} can therefore be thought of as the mixed layer depth if the same BD were redistributed to achieve an unstratified SL, keeping $\Delta\sigma_\theta$ intact (Fig. 2c). For the same BD, small h_{BD} means that the meltwater is accumulated in the PC, and larger h_{BD} means that the meltwater is distributed more evenly with depth. It is also helpful to keep in mind that by definition, h_{BD} is at least 0 m and at most equal to the reference depth (in this case, 50 m).

c. Observed parameter ranges

Pooling all the summer profiles with a sufficient amount of meltwater accumulation in the upper tens of meters ($\Delta\sigma_\theta > 0.02\,\mathrm{kg\,m^{-3}}$ as discussed above), we observed the following parameter ranges (given as median values, with 5% and 95% quantiles in brackets): $\mathrm{BD} = 19\ [7, 40]\,\mathrm{kg\,m^{-2}}$, $h_{\mathrm{BD}} = 20\ [14, 29]\,\mathrm{m}$, and $E_0 = 12\ [0.4, 77] \times 10^{-4}\,\mathrm{kg\,s^{-3}}$ (corresponding to wind speeds of $5.6\ [2.1, 11.4]\,\mathrm{m\,s^{-1}}$). The BD and h_{BD} were not correlated on a survey basis, but a seasonality in $\Delta\sigma_\theta$ leads to a remarkable proportionality when grouped by campaign, that is, by area and time (Fig. 3). This latter relation will be explored in more detail in objective 2.

Surface buoyancy fluxes were in the range 4×10^{-9}–$4 \times 10^{-7}\,\mathrm{W\,kg^{-1}}$; fluxes larger than $10^{-7}\,\mathrm{W\,kg^{-1}}$ were associated with rapidly disintegrating ice floes over the inflowing Atlantic water [melt rates $O(10)\,\mathrm{cm\,day^{-1}}$], whereas more typical melt rates [$O(1)\,\mathrm{cm\,day^{-1}}$] entailed $\langle w'b'\rangle$ below $3 \times 10^{-8}\,\mathrm{W\,kg^{-1}}$ (see also Peterson et al. 2017). Larger $\Delta\sigma_\theta$ was associated with larger $\langle w'b'\rangle_0$ or sampling later in the melt season (Fig. 3c).

d. A predictive model of the vertical density structure and stratification

In a qualitative sense, the vertical density profiles are largely consistent with the general notion that larger amounts of freshwater (i.e., BD) and larger top to deep density differences (i.e., $\Delta\sigma_\theta$) mean stronger overall stratification, while smaller equivalent mixed layer depths (i.e., h_{BD}) mean that the freshwater is accumulated at shallower depths. However, we are interested in quantitative models of the vertical density structure as a function of these easily accessible parameters, ultimately in order to predict the structure of vertical mixing (see objective 3). The method must be generally

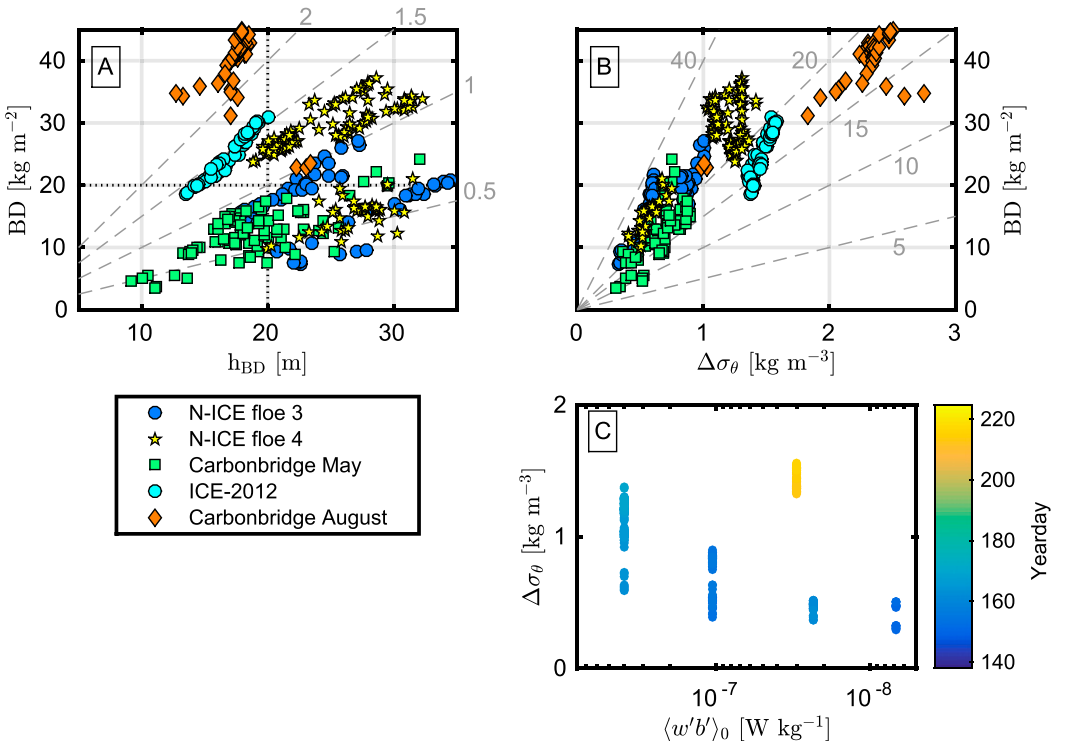

FIG. 3. Parameter range in terms of h_{BD}, $\Delta\sigma_\theta$, BD, and the melt rate. Dashed lines: (a) Lines of constant $\Delta\sigma_\theta$ as indicated by the numbers in the upper-right corner (kg m^{-3}) or (b) h_{BD} (m). Dotted lines in (a) mark the regimes used for grouping data in Figs. 5 and 8. (c) Combined effect of rate and duration of ice melt, here expressed as surface buoyancy flux $\langle w'b' \rangle_0$ on $\Delta\sigma_\theta$.

applicable to vertical stratification profiles, independent of the presence of a mixed layer. Therefore, we have developed a framework that allows computation of the vertical structure from the BD and the equivalent mixed layer depth h_{BD}.

The BD is an easily accessible parameter that is strongly related to the total amount of melt that has happened until the time of sampling. Instead of h_{BD}, one could use $\Delta\sigma_\theta$ as a predictive parameter, as only two of out of BD, h_{BD}, and $\Delta\sigma_\theta$ are independent. We chose h_{BD} for the following reasons: h_{BD} was found to be well correlated with depths where the scaled density coordinate r_σ has specific values (Fig. 4; slopes are close to 1:1). This supports the notion that h_{BD} aptly summarizes the vertical structure of the density profiles. We will also show later (see objective 3) that h_{BD} not only determines the hydrographic structure, but it is also an indicator of the vertical extent of turbulent mixing, that is, the depth from which wind-driven mixing can entrain deeper water into the surface layer.

To determine the relationships between these selected key parameters and vertical profiles of density and turbulent mixing, we employ linear regression models (Fig. 5). For objective 1, we focus on Figs. 5a–f, which treat the dependence of the vertical density structure r_σ and σ_θ and the vertical stability N^2 on BD and h_{BD} (Figs. 5g–n are deferred to the treatment of objective 3). The regressions are performed separately for each depth bin, where depth is binned according to either vertical distance from surface z (Figs. 5b,e) or the density-scaled r_σ coordinate (Figs. 5c,f). The middle and right columns in Fig. 5 thus show how the vertical structure of the quantity in the left column changes as a function of the variable in question (see legends). The vertical coordinate is isobaric, the distance from surface z in the middle column, and based on the scaled depth r_σ in the right column. The use of z that extends to 75 m allows to resolve the SL–PC continuum as well as the structure below the deep reference of 50 m where $r_\sigma = 1$.

For example, in Fig. 5c, we fit a linear model of the form $\sigma_\theta = a + b\,\mathrm{BD} + c\,h_{BD}$ to all the (σ_θ, BD, and h_{BD}) data points in each specific r_σ interval. We then refer, for example, to b as the sensitivity of σ_θ to BD and so forth. Figure 5c shows that in the surface bin, σ_θ is reduced by approximately -0.05 kg m^{-3} per BD increase of 1 kg m^{-2}, which we would describe in our terminology as follows: the sensitivity of surface σ_θ to BD is -0.05(kg m^{-3})/(kg m^{-2}).

Figures 5a and 5d show average profiles of r_σ and N^2, respectively, binned according to BD and h_{BD} associated

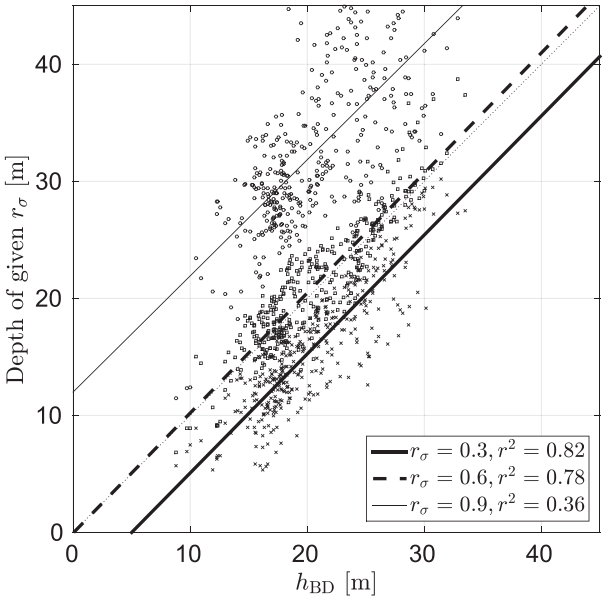

FIG. 4. Relation between h_{BD} and depths of constant r_σ at the levels $r_\sigma = 0.3$ (crosses), 0.6 (squares), and 0.9 (circles). The diagonal lines are linear regressions based on all samples in each category.

with each profile. The remaining panels (Figs. 5b,c,e,f) show regression results, where BD and h_{BD} are the predictor variables and either σ_θ (Figs. 5b,c) or $\log_{10}N^2$ (Figs. 5e,f) is the response variable.

The terms σ_θ, N^2, and r_σ all exhibit well-defined responses to h_{BD} and BD. Interestingly, the vertical structure of the density profiles (as given by r_σ and N^2) did not depend on the total amount of meltwater, that is, BD (Figs. 5a,f). Increasing amounts of freshwater were accumulated mostly in the upper 30 m (Figs. 5b,e).

e. *Summary for objective 1*

Density profiles of the upper water column comprising freshwater layers are characterized by h_{BD}, BD, and $\Delta\sigma_\theta$, any two of which are independent and determine the third by the defining relationship $h_{\mathrm{BD}} \equiv \mathrm{BD}/\Delta\sigma_\theta$. Large accumulations of meltwater entail large BD, whereas high h_{BD} values indicate relatively deep pycnoclines and weakly stratified surface layers. Changes in the BD and h_{BD} values associated with a particular profile are tightly connected to changes in the density structure of that profile; the shape of the r_σ profile is largely determined by h_{BD}, revealing a certain amount of generality across all density profiles in our dataset.

4. Objective 2: Seasonal evolution and asymptotic states of freshwater layers in the IOBL

In Fig. 3, two features emerged: the relatively narrow $\Delta\sigma_\theta$ range that was observed during each of the campaigns, and the narrowing range of observed h_{BD} values as the melt season progresses and BD increases going into July and August.

In the following, we argue that neither of these features is a coincidence. However, while convergence to specific h_{BD} values can in fact be explained as the asymptote of a simple evolution equation, the apparent convergence to relatively narrow ranges of $\Delta\sigma_\theta$ requires more elaboration.

a. *Seasonal evolution toward asymptotic* h_{BD}

As will be shown below in our discussion of objective 3, h_{BD} plays an important role in regulating the maximum vertical extent of wind-driven mixing. This warrants an attempt to understand its seasonal dynamics. From the definition of h_{BD}, we can derive a simple expression for its temporal evolution:

$$\partial_t h_{\mathrm{BD}} = \partial_t\left(\frac{\mathrm{BD}}{\Delta\sigma_\theta}\right) = \frac{1}{\Delta\sigma_\theta}(\partial_t \mathrm{BD} - h_{\mathrm{BD}}\partial_t\Delta\sigma_\theta). \quad (1)$$

Now the problem is reduced to specifying how BD and $\Delta\sigma_\theta$ evolve. The former is straightforward and follows from integrating the melt rate. The temporal evolution of $\Delta\sigma_\theta$ is governed by the divergence of the buoyancy flux through a small control volume of thickness z^* (e.g., 2 m, such that it could cover the 3–5-m depth interval used to calculate the upper density $\sigma_{\theta 0}$ in this study) at the ice–ocean interface. The flux leaving this control volume upward is simply the melt rate $\langle w'b'\rangle_0$. The flux entering the control volume at a distance z^* from the ice–ocean interface is denoted by $\langle w'b'\rangle_{z^*}$. The rate of change of $\Delta\sigma_\theta$ is then the result of a simple budget:

$$\partial_t\Delta\sigma_\theta = \frac{\rho_w}{g}(\langle w'b'\rangle_0 - \langle w'b'\rangle_{z^*})/z^*. \quad (2)$$

Both $\partial_t\mathrm{BD} \propto \langle w'b'\rangle_0$ and $\partial_t\Delta\sigma_\theta$ are positive through the season, as BD and $\Delta\sigma_\theta$ both increase as the melt season progresses (Fig. 3). Under these conditions, the asymptote of the exponential evolution equation (1) is well defined:

$$h_{\mathrm{BD}}^{\infty} = \frac{\partial_t\mathrm{BD}}{\partial_t\Delta\sigma_\theta} = z^*\frac{\langle w'b'\rangle_0}{\langle w'b'\rangle_0 - \langle w'b'\rangle_{z^*}}, \quad (3)$$

where the last equality follows from inserting Eq. (2). From Eq. (3), we can see that increasing $\langle w'b'\rangle_0$ means decreasing h_{BD}^{∞} as $\langle w'b'\rangle_{z^*}$ is not strongly dependent on the melt rate. The time scale for the exponential convergence is $\Delta\sigma_\theta/\partial_t\Delta\sigma_\theta$. Later in the melt season, this time scale can be several weeks (based on an increase from $\Delta\sigma_\theta \approx 1.2$ to 1.4 kg m^{-2} during the 1-week drift of ICE-2012). However, early in the season, when $\Delta\sigma_\theta$ is small,

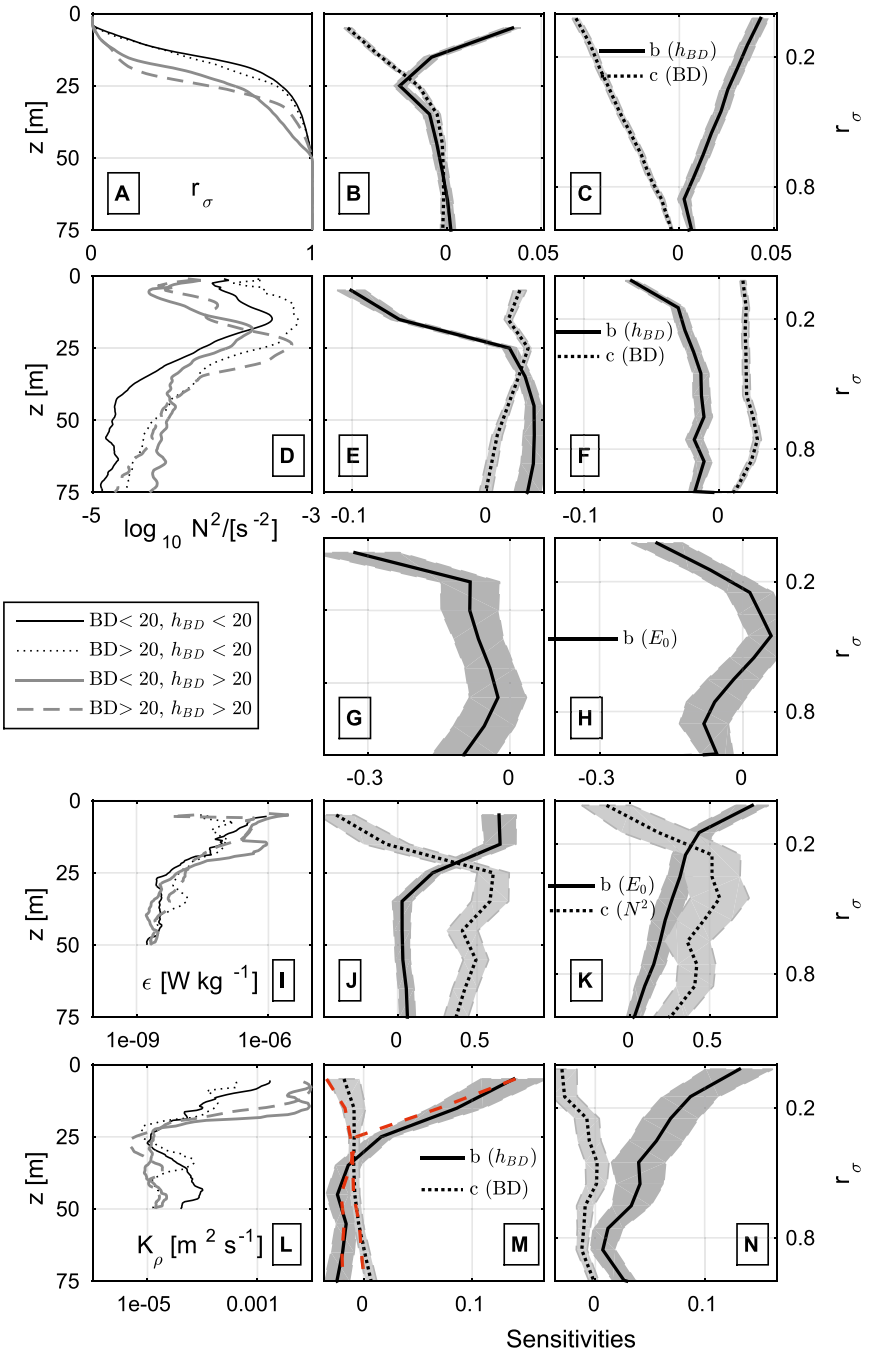

FIG. 5. Mean profiles of r_σ, N^2, ε, K_ρ, and the sensitivities of σ_θ, N^2, ε, and K_ρ to various parameters (see legend), as quantified from a linear regression for each subset of observations in vertical bins (distance from surface, z, or scaled density r_σ). (left) Mean profiles. (center) Profiles of sensitivities plotted against physical depth. (right) Profiles of sensitivities plotted against r_σ. Differences between the second and third column are due to implicit dependencies of r_σ on N^2, σ_θ, and so on. (a),(d),(i),(l) Mean profiles of r_σ, N^2, ε, K_ρ, respectively, binned according to their associated h_{BD} and BD values. (b),(c) Sensitivity of σ_θ to h_{BD} and BD (b and c in $\sigma_\theta = a + b\,h_{\mathrm{BD}} + c\,\mathrm{BD}$). (e),(f) Sensitivity of N^2 to h_{BD} and BD (b and c in $\log_{10}N^2 = a + b\,h_{\mathrm{BD}} + c\,\mathrm{BD}$). (g),(h) Sensitivity of N^2 to E_0 (b in $\log_{10}N^2 = a + b\log_{10}E_0$). (j),(k) Sensitivity of ε to E_0 and N^2 (b and c in $\log_{10}\varepsilon = a + b\log_{10}E_0 + c\log_{10}N^2$). (m),(n) Sensitivity of K_ρ to h_{BD} and BD (b and c in $\log_{10}K_\rho = a + b\,h_{\mathrm{BD}} + c\,\mathrm{BD}$). Red lines in (m) indicate the sensitivities inferred using (j) and (e) as described in section 5. The shaded areas are 95% confidence intervals from the fit, which is linear in every predictor variable mentioned in each panel.

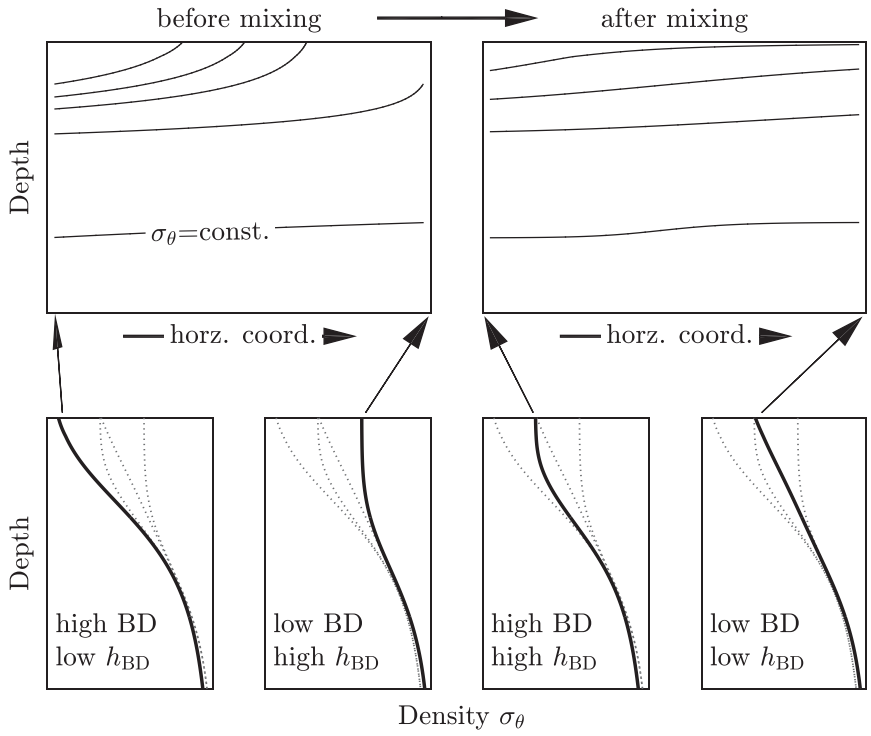

FIG. 6. Hypothetical mixing process that could explain the observed narrow $\Delta\sigma_\theta$ ranges while preserving a large range of BD values. If horizontal mixing in the very surface is much stronger than mixing at depths of a few tens of meters, this generates profiles with very similar $\Delta\sigma_\theta$ but a wide range of BD and accordingly h_{BD} values. (top) Contours of constant $\Delta\sigma_\theta$ as function of depth and the cross-front horizontal coordinate (left) before and (right) after mixing has taken place. (bottom) Conceptual profiles at either side of the front, both before and after mixing, with the respective profile in bold and the other profiles dotted.

this convergence is fast (days), such that we can stipulate that the actual h_{BD} is close to h_{BD}^{∞} as long as no abrupt, big changes in melt rates or turbulent mixing have occurred. The shoaling and narrowing of the observed range of h_{BD} values is thus a consequence of Eq. (3), where increasing melt rates only allow for smaller ranges of h_{BD} values.

b. *Ice–ocean interface buoyancy flux and the regional convergence of* $\Delta\sigma_\theta$

Higher melt rates should entail both shallower stratification and larger accumulations of meltwater (i.e., $h_{BD} \sim 1/BD$). However, Fig. 3a suggests that for each of the data clouds (each of which are, on a per campaign basis, geographically well-separated and hydrographically diverse; not shown), shallower stratification actually coincides with smaller amounts of freshwater (i.e., $h_{BD} \sim BD$). One might imagine that this is part of a feedback mechanism whereby higher melt rates introduce more meltwater and increase shallow stratification, thereby reducing the melt rate (see, e.g., Randelhoff et al. 2014). However, this would likely lead to a convergence to common (regional) melt rates rather than a common $\Delta\sigma_\theta$ value (Fig. 3b). Indeed, it seems to be a combination of the melt rate and the total duration of the melt that drove the evolution of $\Delta\sigma_\theta$ in our dataset (Fig. 3c). We propose instead that lateral mixing might explain the observed parameter behavior ($h_{BD} \sim BD$).

Gravitational slumping of fronts (i.e., gravitational flattening of isopycnals), where the heavier water slides underneath the lighter water, has been observed in the Arctic Ocean both in winter under sea ice (Timmermans et al. 2012) and in meltwater-induced fronts in the Chukchi Sea (Timmermans and Winsor 2013). For our dataset, slumping alone cannot explain the apparent discrepancy between the $h_{BD} \sim BD$ distribution observed in the field and the $h_{BD} \sim 1/BD$ distribution conjectured based on one-dimensional boundary layer physics as detailed above. However, slumping combined with the observed, vertically rapidly attenuated diapycnal mixing could produce a vertical structure of lateral mixing sufficient for explaining the observations (Fig. 6). This mechanism would mix the stratified upper surface waters more strongly than waters at depths of a

few tens of meters, and thus the result would be two density profiles that have similar densities at the surface and at ~50-m depth, but different densities in the pycnocline (i.e., similar $\Delta\sigma_\theta$ but varying BD; see lower panels in Fig. 6).

c. Summary for objective 2

We found clear patterns in the temporal evolution of density profiles in h_{BD}–BD–$\Delta\sigma_\theta$ parameter space. Our results indicate that profiles from a certain region and time of the year exhibit very similar upper densities $\sigma_{\theta 0}$, which hints at the importance of lateral mixing processes. As the melting season progresses, the surface layer becomes lighter and stratification (i.e., the equivalent mixed layer depth h_{BD}) shoals and becomes less variable. Consistent with observations, h_{BD} is conjectured to converge to a constant value set by ice melt and ice–ocean interface turbulence.

5. Objective 3: Vertical mixing

The previous sections suggest that the evolution of sea ice meltwater layers is governed by robust patterns, many of which can be quantified. What is still missing in order to assess the role they play in shaping the current and future Arctic is how these meltwater layers affect the vertical extent and intensity of turbulent mixing.

a. Mixing parameters

A mixing layer depth h_ε is defined as the depth to which active turbulence mixing induced by surface processes reaches (Brainerd and Gregg 1995), inducing buoyancy flux through entrainment. The term h_ε is distinct from and can be shallower or deeper than the mixed layer depth (which we have not defined or used in this study). Dissipation rate profiles can be used to estimate h_ε. Here, we define h_ε as the shallowest depth where the 5-m smoothed dissipation rate drops below $5 \times 10^{-9}\,\mathrm{W\,kg^{-1}}$. The dissipation threshold must be several orders of magnitude less than the energetic upper layer and close to the deep background values (e.g., Fig. 5i). The values of h_ε are not sensitive to the exact choice of the threshold, since the dissipation rate decays rapidly with depth from the turbulent surface layer.

Regarding the intensity of the turbulent mixing, several quantities are of interest. The rate of dissipation of turbulent kinetic energy is measured by vertical microstructure profilers recording small-scale shear ($\mathrm{W\,kg^{-1}} \equiv \mathrm{m^2\,s^{-3}}$). As such, it describes turbulence in an energetic sense since its vertical integral over the mixing layer approximately balances the turbulent kinetic energy supplied through the surface layer and expended on the upward buoyancy flux. The vertical mixing of tracers, on the other hand, is described by the eddy diffusivity K_ρ, frequently parameterized as $K_\rho = \Gamma(\varepsilon/N^2)$ (Osborn 1980). While the magnitude of the coefficient Γ depends on multiple parameters, in this study we use the canonical value of 0.2 that has been found to be appropriate for long-term averages in stratified regions (Osborn 1980; Moum 1996). Also note that Sundfjord et al. (2007) provided support for this value for diffusively stable conditions in their data from the MIZ of the Barents Sea. Given an unchanged background E_0 and Γ, the relative changes in K_ρ are mostly governed by the dependency of ε on N^2, which is governed by BD and h_{BD} (see objective 1), which in turn are governed by robust seasonal patterns (see objective 2). With this in mind, we now turn our attention to the effect of meltwater layers on upper-ocean turbulent mixing.

b. Scaling of dissipation rate and diffusivity

Figures 7a and 7b show dissipation in the SL, the PC, and deep layer as a function of in situ buoyancy frequency and wind forcing. In the SL, ε was significantly elevated above deep ε, decreased with increasing N^2, and increased with increasing E_0. The observations are typical of earlier studies and are intuitive. The decrease in ε with increasing N^2 still holds when looking at specific fixed-depth intervals (not shown). In the PC, dissipation levels were drastically reduced from SL values but remained slightly higher than deep dissipation values. Increasing E_0 led to the steepest increase in ε in the SL and was negligible below the PC.

Deep surface mixed layers and mixing depths in excess of 60 m were observed (Fig. 8a) during neutral or slightly unstable stratification in the N-ICE2015 January data. For strong wind forcing, h_ε during shallow stratification was reduced by several tens of meters relative to the deep mixed layers. Across both meltwater layers and deep mixed layers, h_ε increased with higher wind speeds as expected. The profiles with a meltwater layer, however, show no significant change in the dependency of h_ε on E_0 for changes in BD and h_{BD} (Fig. 8a). Indeed, h_{BD} was limiting for h_ε only in cases of strong wind; during times of low E_0, h_ε was, on average, half the value of h_{BD} (Fig. 8b).

We now extend the depth-binned linear regression analysis from objective 1 (section 3) to turbulence parameters, displayed in Figs. 5g–n. Briefly, for each depth bin, we determined the regression slopes of the response variable ($\log_{10}N^2$, $\log_{10}\varepsilon$, or $\log_{10}K_\rho$) as a linear function of one or two predictor variables. In the following, sensitivity refers to this slope, but to avoid cluttering the description, log transformations may be implied (e.g., sensitivity of ε will refer to that of $\log_{10}\varepsilon$). See the figure caption of Fig. 5 for the exact definitions of the regression equations.

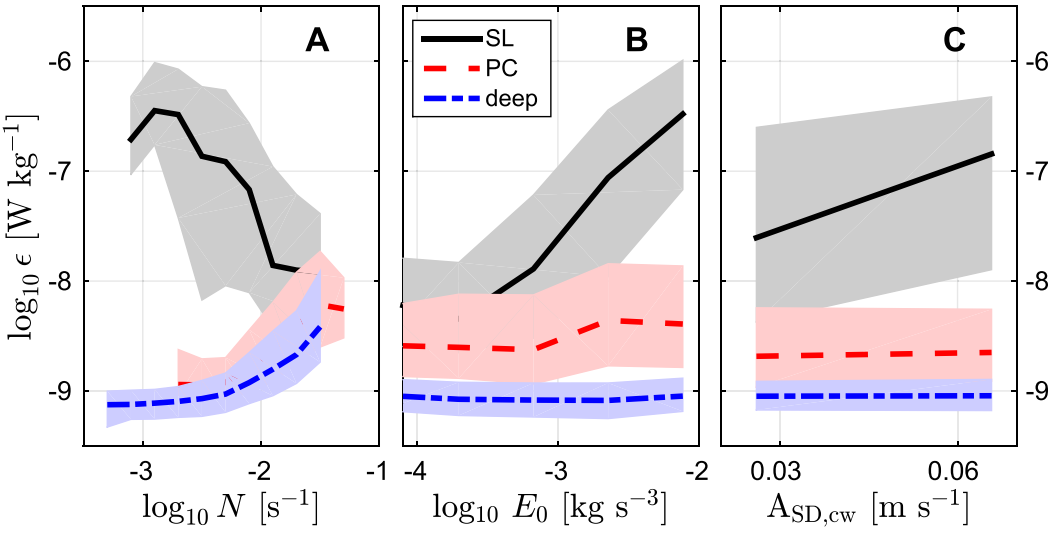

FIG. 7. Dissipation rates $\log_{10}(\varepsilon)$ as a function of (a) stratification N, (b) wind work E_0, and (c) amplitudes of near-inertial motions, grouped according to SL, PC, and deep (below PC); for definitions, see section 3a. Shading indicates the respective first and third quartiles.

Instantaneous wind work had the largest effect on ε (as scaled by the ranges of the predictor variables) in the surface and down to $r_\sigma \approx 0.3$, reaching zero at $r_\sigma \approx 1$ or $z \approx 35$ m (Figs. 5j,k). This is not to say that wind energy generally did not penetrate below this depth, but the instantaneous surface wind was not coherent with ε below that level anymore. Sensitivity of ε to N^2 was around zero, at most slightly negative, in the surface, reaching a constant $\varepsilon \propto (N^2)^{0.5}$ exponent from $r_\sigma = 0.3$ and deeper (Figs. 5j,k).

The BD and h_{BD} affected K_ρ down to $r_\sigma = 0.5$ or about 30 m; K_ρ increased with increasing h_{BD} and slightly with decreasing BD (Figs. 5m,n). The BD had its largest effect in the PC (Fig. 5n), where it increased stratification (Fig. 5f). Increasing h_{BD} was related to weakening surface layer stratification (Fig. 5f), which is connected to higher E_0 values (Fig. 5g). As a reality check of this sensitivity approach, we can also estimate

$$\frac{\partial \log_{10} K_\rho}{\partial \mathrm{BD}} \approx \left(\frac{\partial \log_{10} \varepsilon}{\partial \log_{10} N^2} - 1 \right) \frac{\partial \log_{10} N^2}{\partial \mathrm{BD}}$$

(and analogously for h_{BD}). The approximate equality stems from the fact that

$$\frac{\partial \log_{10} \varepsilon}{\partial \mathrm{BD}} \approx \frac{\partial \log_{10} \varepsilon}{\partial \log_{10} N^2} \frac{\partial \log_{10} N^2}{\partial \mathrm{BD}},$$

neglecting implicit dependencies other than that on the dominant factor N^2; $\partial \log_{10}\varepsilon / \partial \log_{10} N^2$ is then taken from Fig. 5j and $\partial \log_{10} N^2 / \partial \mathrm{BD}$ is taken from Fig. 5e. The patterns and magnitudes in the resulting sensitivity estimates are remarkably similar (Fig. 5m) when considering that the above approximation neglects the wind speed, which likely leads to some residual (nonlinear) effects due to its correlation with upper-ocean stratification (Fig. 5g).

c. *Effects of presence or absence of ice cover*

Sea ice can affect turbulent mixing in the ice–ocean turbulent boundary layer in two ways: 1) directly altering air–sea interaction, by, for example, changing air–sea into air–ice drag, suppressing surface gravity waves, breaking of surface waves, inhibiting Langmuir circulation, and so on, and 2) changing the underice stratification by acting as a strong buoyancy source (ice melt). Since the effects of issue 2 are easily quantifiable in the BD – h_{BD} framework, we seek to isolate issue 1 and compare vertical profiles of dissipation with and without ice cover.

Based on our previous discussion, we suspect the largest changes in the vertical structure of dissipation are linked to variations in h_{BD} and BD. However, h_{BD}, BD, and E_0 all cover a similar range of values and do not seem to be related to systematic changes in the relative structure of $\varepsilon(z)$ between open-water and ice-covered conditions. Stations over the shelf frequently exhibited other mixing processes like tidal and frontal mixing, possibly in connection with the shallow topography, leading to interleaving and complicated vertical structures in dissipation profiles that we are confident do not reflect surface-driven mixing (not shown). (Note, however, that these additional processes mostly affected the open-water stations since the ice-covered stations were mostly located off shelf.) Thus, considering only profiles at bottom depths of >500 m, this leaves us with

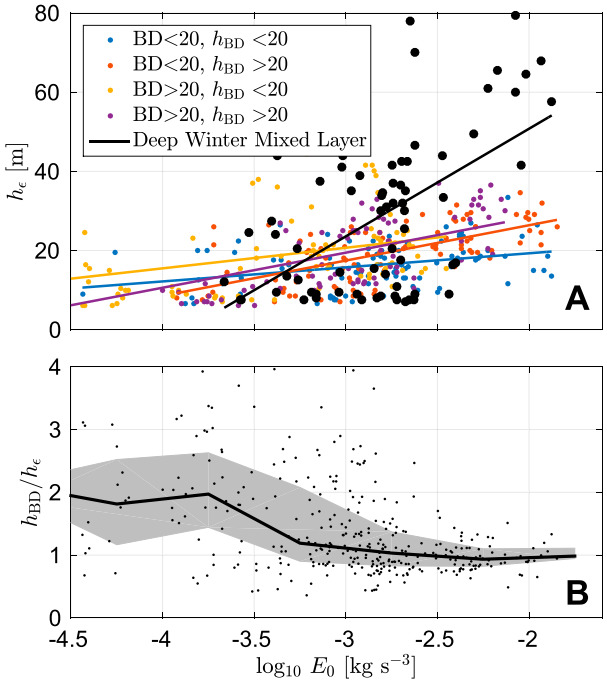

FIG. 8. (a) Mixing layer depth h_ε as function of wind work E_0. Colored dots and regression lines refer to meltwater affected profiles, binned according to their associated h_{BD} and BD values. Black dots and regression lines refer to deep wintertime mixed layers. (b) Discrepancy between equivalent mixed layer depth h_{BD} and mixing layer depth h_ε as a function of wind work E_0. Shaded area and thick line indicate quartiles and median, respectively.

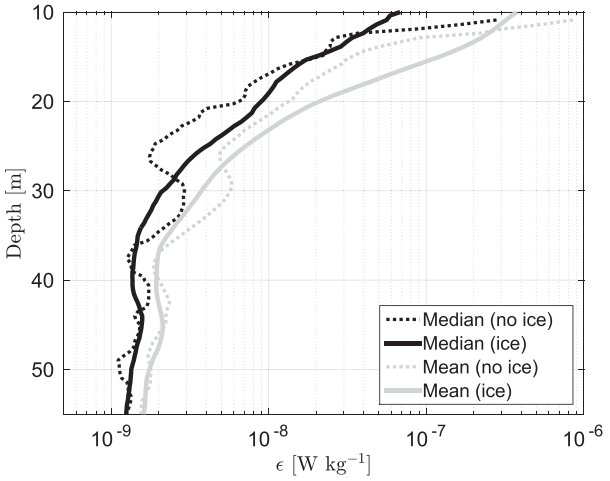

FIG. 9. Vertical profiles of median (black) and maximum likelihood estimates of mean (gray) dissipation rates at ice-covered (solid) and open-water (dotted) stations; see the text for details of the subsampling. Sample sizes: open water (n = 30), ice cover (n = 170).

30 profiles under open water and 170 profiles under ice-covered conditions. Neither mean (maximum likelihood estimates using a lognormal estimator) nor median dissipation profiles show any significant deviation between the presence and absence of ice cover (95% confidence intervals approximately ±20%; Fig. 9).

We conclude that the purely surface-driven (i.e., wind driven) part of the $\varepsilon(z)$ profile is probably not affected by the presence or absence of sea ice. Additional regional factors can likely change the vertical structure; however, these were not present in our dataset away from the influence of shallow topography over the shelf. This means that sea ice alters vertical mixing first and foremost in the form of K_ρ via stronger and shallower stratification. Note, however, that most of our stations were conducted in the highly mobile ice of the MIZ; the interior ice pack might shield the ocean underneath better from wind energy input.

d. Near-inertial energy

Near-inertial energy input from wind stress can lead to turbulence in the upper ocean through several mechanisms including bulk shear spiking, modulation of near-inertial shear and strain to allow conditions favorable for turbulence production, and breaking of near-inertial internal waves.

Following a storm event in the Amundsen Basin in the central Arctic Ocean, Fer (2014) found that dissipation averaged in the pycnocline was near-inertially modulated and decayed approximately at a rate implied by the reduction of near-inertial energy over time. In contrast, in the Canada Basin, where the surface layer stratification was substantially stronger than the Amundsen Basin, Lincoln et al. (2016) observed that despite unusually ice-free and stormy conditions, turbulence was not energetic below the stratified upper layer.

Diagnosis of input and fate of near-inertial energy requires detailed observation of upper-ocean current time series. These are not available for most of our microstructure data nor are the analyses of isolated high-energy events practical in a bulk statistics methodology as we employ in this study. We therefore refrain from general inferences about near-inertial mixing in the seasonal pycnocline, but in light of the still unclear role of near-inertial energy in mixing the upper ocean, a few remarks are worthwhile.

In our data, near-inertial energy can be inferred from the amplitude of the clockwise semidiurnal component of the ice velocity $A_{SD,cw}$. In the data analyzed here, these amplitudes are rather small (ranging between 0.005 and 0.08 m s^{-1}) and near-inertial oscillations are seen to enhance dissipation rates in the surface layer ($r_\sigma \leq 0.2$) but not below (Fig. 7c). The presence of inertial oscillations often coincided with stronger winds during N-ICE2015 (not shown), which can also account for the increase in SL dissipation levels. As most of the ice–ocean shear should be

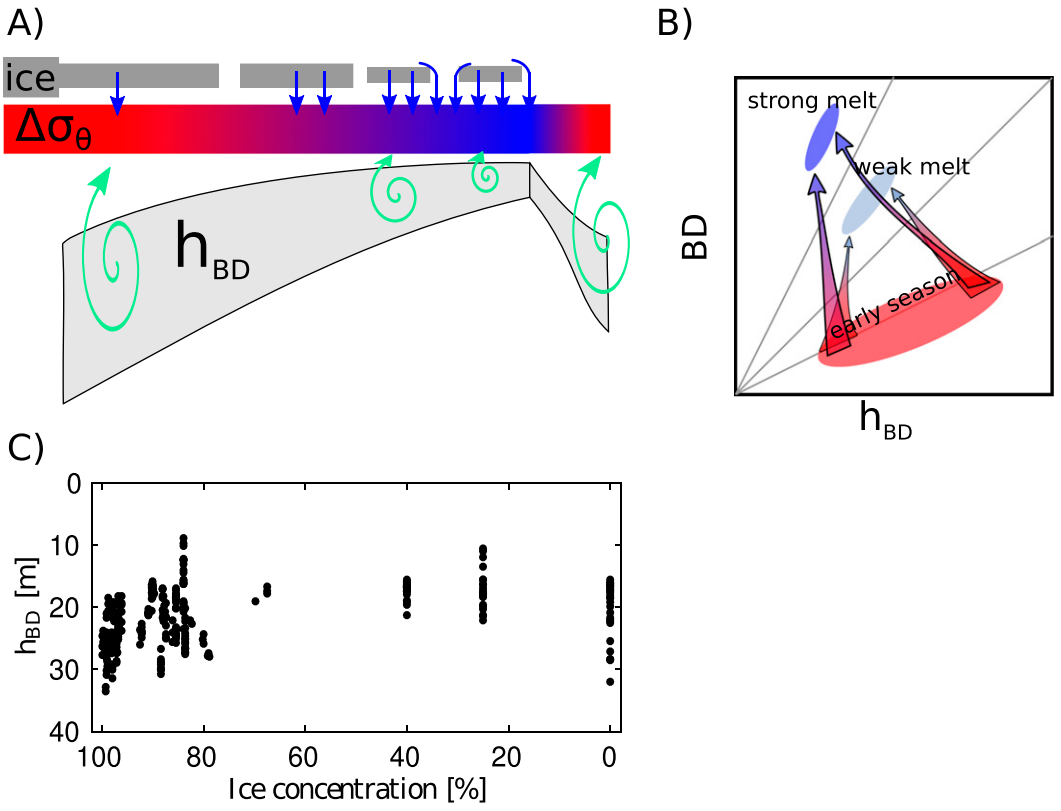

FIG. 10. Sketch of the conceptual model. (a) Blue arrows indicate meltwater input. The color gradient indicates small (red) to large (blue) surface buoyancy deviations $\Delta\sigma_\theta$. Light gray indicates the range of equivalent mixed layer depths h_{BD}, narrowing and shoaling as melt rates increase. When the ice vanishes, h_{BD} deepens again and $\Delta\sigma_\theta$ decreases. Green whirls indicate that mixing depth h_ε is constrained by h_{BD}. (b) Evolution in BD–h_{BD} parameter space (cf. Fig. 3). Darker blue indicates higher melt rate, which leads to higher BD and lower h_{BD} later in the season. (c) h_{BD} vs sea ice concentration as observed in the field, inferred from Advanced Microwave Scanning Radiometer 2 (AMSR2) using the Arctic Radiation and Turbulence Interaction Study (ARTIST) Sea Ice algorithm (downloaded from https://seaice.uni-bremen.de/data/amsr2/; Spreen et al. 2008).

located in the PC, near-inertial shear spiking was probably not an important turbulence generation mechanism in the seasonal pycnocline of the MIZ as observed from late May onward on the N-ICE campaign.

e. *Summary for objective 3*

The vertical extent of the mixing layer is regulated by the accumulation of meltwater in the IOBL. The equivalent mixed layer depth h_{BD} is an approximate upper bound for the mixing layer depth h_ε, and the two are approximately equal for sufficiently strong wind ($E_0 > 10^{-3}\,\mathrm{kg\,s^{-3}}$). In addition, both h_{BD} and the buoyancy deficit BD are strongly affected by stratification, which influences the magnitude and vertical structure of ε and K_ρ.

The presence or absence of sea ice did not have a discernible impact on the intensity and vertical structure of surface-driven turbulent mixing. However, since sea ice is the source of a continuous meltwater flux, stratification under sea ice is generally stronger and h_{BD} values are smaller, which leads to shallower mixing layers and decreased eddy diffusivities K_ρ. Within the limitations of our dataset, we can further state that near-inertial shear (localized in time and space) was not found to generate enhanced mixing in the seasonal pycnocline.

6. Synthesis

a. *A conceptual model of mixing in summertime meltwater layers*

Before quantifying how the dissipation profiles react to changes in different key variables, we interpret the previous section's results and distill them into a qualitative model of how upper-ocean stratification evolves after the onset of the melt season (Fig. 10). The positive buoyancy flux (increasing BD) from ice and snowmelt simultaneously freshens the surface layer (increasing $\Delta\sigma_\theta$) and shoals the pycnocline (decreasing h_{BD}).

In the upper 10 m, mixing is dominated by wind-generated shear (Fig. 5j). The fact that $\varepsilon \propto N$ both in

the PC and below is consistent with dissipation of a single-frequency or narrowband internal wave, such as near-inertial internal waves. This scaling corresponds to type 1 of Gargett and Holloway (1984) who suggest that waves of a single-frequency (or narrowband) scale as $\varepsilon \propto N^{+1}$ (as opposed to a Garrett–Munk-like internal wave field, which scales as $\varepsilon \propto N^{+1.5}$, their type 2). In the SL, similar breaking of near-inertial waves at stronger stratification might be offset by enhanced penetration of wind work at weaker stratification, but evidence remains inconclusive because of many correlated variables. Note that internal wave spectra in the Arctic Ocean have been found to deviate from the Garret–Munk form (D'Asaro and Morison 1992; Fer et al. 2010). Vertical wavenumber spectra of horizontal velocity are a factor of 10–100 below the midlatitude spectra at low wavenumbers but are comparable in magnitude and slope at high wavenumbers where the spread is less. This indicates a tendency toward a common scaling at small scales where dissipation occurs.

The specifics of the recent E_0 and $\langle w'b' \rangle_0$ forcing then dominate h_{BD} (speculatively, on time scales of weeks), which determines the freshwater distribution, while the temporal seasonal integral of $\langle w'b' \rangle_0$ (which is proportional to the BD accumulated up until that point) does not influence the shape of the density profile. This explains that BD $\propto N^2$ and together with $\varepsilon \propto N$ means that as the melt season progresses, the upward turbulent flux of buoyancy through the PC ($\langle w'b' \rangle \approx 0.2\varepsilon$) increases steadily while $K_\rho \approx 0.2\varepsilon/N^2$ decreases.

b. Future summertime mixing in the upper ocean

The years 2007, 2011, and 2012 saw the lowest September minimum extent of Arctic sea ice since the beginning of satellite observations of the Arctic ice cover. As the Arctic sea ice cover shrinks and thins (Stroeve et al. 2012), the ice–albedo effect will drive higher melt rates. Thus, the main parameter driving changes in the summertime IOBL will be the melt rate $\langle w'b' \rangle_0$ and, to a lesser extent, the seasonally integrated melt BD.

The sensitivity of K_ρ to varying BD and h_{BD} that we determined in section 5 summarizes the status quo. Randomly selecting two profiles from our dataset with different h_{BD} and BD values, their relative difference in $K_\rho(z)$ would, on average, be determined by these sensitivities. However, if the average melt rate increased, we could expect that the temporal evolution of the density profiles changes, taking a different route in BD–h_{BD} parameter space altogether. In particular, with an increase in $\Delta\sigma_\theta$, we can expect h_{BD} to decrease and BD to increase relative to a lower melt rate after the same amount of time elapsed after the onset of melt (cf. cases of weak and strong melt in Fig. 10b).

However, there are no indications that a change in average melt rates would change the diversity of h_{BD} values encountered early in the season. Thus, along lines of constant $\Delta\sigma_\theta$, the bulk of the profiles in our dataset and under higher melt rates would overlap with each other and lead to little change early in the season. The main difference would be that higher values of $\Delta\sigma_\theta$ would be reached earlier. Late in the season, it will become noticeable that the asymptotic h_{BD}^{∞} decreases as melt rates increase and that the overall BD is larger (see Fig. 10b). Both of these factors contribute to decreasing K_ρ.

McPhee et al. (1998) noted a seasonally integrated freshwater addition of 0.8 m (BD $\approx 20\,\mathrm{kg\,m^{-2}}$) during the Arctic Ice Dynamic Joint Experiment (AIDJEX) campaign (1975) in the Beaufort Gyre. This figure is consistent with the roughly 0.6 m of freshwater equivalent of seasonal ice melt Timmermans et al. (2011) give for the years 2007–10 in the Eurasian Basin. Taking the maximum BD $\approx 45\,\mathrm{kg\,m^{-2}}$ of our dataset would indicate a hypothetical difference of $(\partial \log_{10} K_\rho/\partial \mathrm{BD})\Delta\mathrm{BD} \approx -0.02(45 - 20) = -0.5$, that is, K_ρ at 20-m depth in the MIZ in late summer is possibly a factor of 3 lower than in the interior ice pack. Therefore, even though insolation often leads to higher water temperatures in the MIZ and therefore larger vertical heat fluxes, some, if not all, of the effect of this temperature increase might be offset by a corresponding decrease in K_ρ.

An additional complication is that when melt rates are high enough to melt all the ice before the end of the melting season, open-water processes might play a role late in the season. However, as we showed above for the MIZ, the main difference between the presence and absence of sea ice lies in fact primarily in that sea ice is a buoyancy source and supplies a positive $\langle w'b' \rangle_0$. The absence of such a buoyancy flux then likely leads to deepening h_{BD}, decreasing overall N^2 and thus increasing K_ρ. Quantifying these processes will require more dedicated measurements that resolve the late-season and open-water variability.

c. Implications for the Arctic marine ecosystem

Photosynthesis can only take place in the sunlit part of the water column, which in the Arctic Ocean means the uppermost tens of meters (e.g., Stein and MacDonald 2004). Just as spring stratification and the associated reduction in vertical eddy diffusivity likely play a role in timing of underice algal blooms (see the critical mixing hypothesis; e.g., Huisman et al. 1999), increased water column stability will limit the resupply of nutrients from below. The present study is therefore of immediate interest to understanding the upper-ocean ecosystem in polar waters.

Note that even though K_ρ decreases as the melt season progresses, this does not strictly imply a reduction in the vertical fluxes of tracers feeding into the meltwater layer. In the course of the season, the concentration gradients over which the fluxes are calculated might move to a level below the pycnocline where stratification is not as strong. Comparing Figs. 5d and 5l, one sees that K_ρ remains constant immediately below the seasonal pycnocline. For instance, as the season progresses, the nitracline moves downward, such that vertical nitrate fluxes are relatively invariant with respect to time within the productive season (Randelhoff et al. 2016).

If the ice cover vanishes from some region toward the end of melt season, deepening h_{BD} will allow the entrainment of nutrients into the surface layer. Thus, the fall blooms in the Arctic Ocean recently observed by Ardyna et al. (2014) may well be linked to the receding ice cover through changes in hydrography, not necessarily through enhanced light input that results from the absence of sea ice.

d. Arctic-wide applicability and limitations

A few notes on the applicability of these results to other parts of the Arctic Ocean are in order. Two types of hydrographic scenarios occur commonly in the Arctic Ocean: 1) In the Boundary Current along the shelf slope, presence of saline Atlantic Water near the surface enables thermal convection. Also the Arctic shelf seas tend to be vertically homogeneous at the end of winter due to haline convection and relatively strong (e.g., tidal) mixing. Similarly, in most of the deep Eurasian Basin (Atlantic–Arctic water masses), winter mixed layers are deep (mostly well below 50 m; see, e.g., Rudels et al. 2004). Thus, the perennial pycnocline does not interfere with the development of a shallow seasonal pycnocline as detailed here. The remnant of the previous winter's mixed layer then provides a convenient way to define the reference level ($r_\sigma = 1$). 2) In the Pacific sector of the Arctic Ocean and in particular in the deep Canadian Basin, the upper ocean is strongly stratified, both throughout the year and far beyond the extent of the seasonal input of meltwater.

The rationale behind the approach taken for our dataset was that most of the boundary layer shear is accumulated in the shallow and strong pycnocline (cf. Randelhoff et al. 2014) and that the reference level $r_\sigma = 1$ therefore represents a natural scale of the limits to the vertical extent of wind-driven turbulent mixing. When the underlying perennial stratification is comparably strong, this vertical scale is not obvious from the density profile alone.

The study by Timmermans et al. (2011) provides a suitable set of test scenarios to explore the challenges for our formalism across scenarios 1 and 2, for example, the distinction between eastern and western Arctic water masses, with the latter strongly stratified below the seasonal meltwater accumulation, the former only weakly. Based on ice-tethered profiler (ITP) data, Timmermans et al. (2011) found that owing to large-scale shifts in atmospheric circulation (cf. Arctic high) in 2009–10, the western Eurasian Basin was populated by strongly stratified water masses from the western Arctic (our scenario 2), whereas in 2007–08, the stratification was more similar to what is commonly found in the eastern Eurasian Basin (our scenario 1). This is shown by profiles sampled between 87.5° and 86°N during summertime by ITPs 7 (2007) and 38 (2010) (Fig. 11a). The vertical structure and the h_{BD}–BD parameter space for the ITP 7 data (Fig. 11b) are similar to what we have described in this study, consistent with the stipulations above, and shows the discussed evolution in h_{BD}–BD space as the season progresses. For the ITP 38 data, the mean hydrographic profile shows that melt rates have not lead to a significant accumulation of meltwater in the upper tens of meters. Therefore, no obvious reference depth can be inferred from the density profile. Arbitrarily choosing 50 m as a reference depth for ITP 38 purely for illustrative purposes, we find that the temporal evolution in h_{BD}–BD space now looks convoluted and in fact is mostly dominated by lateral, nonseasonal changes in hydrography as ITP 38 drifted south toward Fram Strait (Fig. 11c). This is not a shortcoming of our framework itself, but it does demonstrate that the seasonal meltwater cycle might not dominate the near-surface freshwater inventory in the interior ice pack. Our findings are thus mostly applicable in the seasonal ice zone where leads and the ice–albedo feedback can lead to high melt rates. Note, however, that this seasonal ice zone has been expanding in recent decades (Stroeve et al. 2012), which could lead to strengthening of seasonal stratification also in the central Arctic Ocean that has not been subject to large melt rates previously.

7. Summary and perspectives

While it is generally agreed that meltwater layers occurring during the Arctic summer affect air–ice–sea interaction in a number of important ways, a quantitative description has so far been lacking. We have shown that their vertical density structure can be described in terms of three parameters, $\Delta\sigma_\theta$ (surface density deviation), h_{BD} (equivalent mixed layer depth), and BD (buoyancy deficit), two of which are independent. These parameters integrate the total amount of buoyancy deficit due to the meltwater the upper ocean has received and its vertical distribution. Turbulent dissipation and vertical

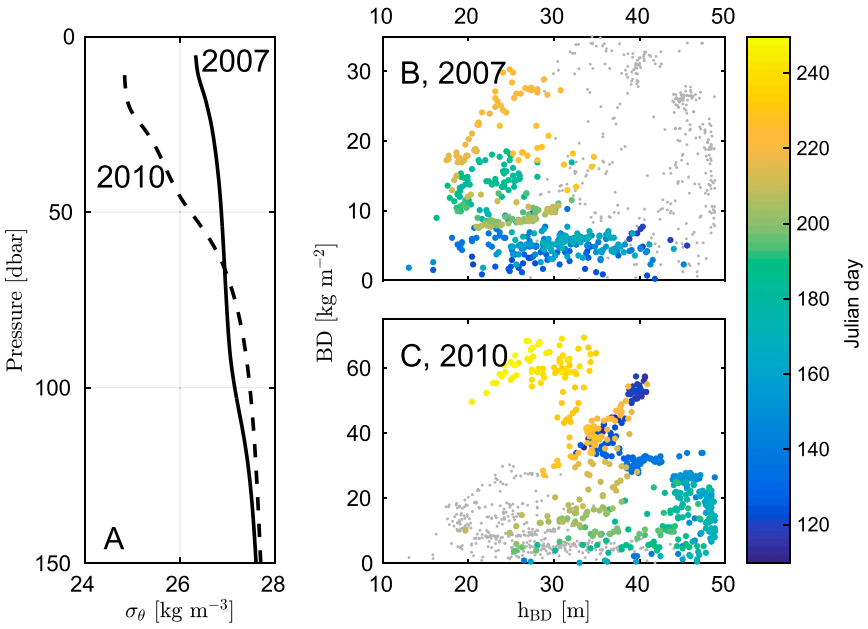

FIG. 11. Ice-tethered profiler data. (a) Average density profiles sampled between 87.5° and 86°N in 2007 (ITP 7) and 2010 (ITP 38). (b),(c) h_{BD}–BD characteristics (see also Fig. 3) from profiles located above 85°N. Both are based on a reference depth of 50 m, which is robust for 2007; for 2010, the results are sensitive to this (mainly illustrative) choice. The gray dots in (b) and (c) show the data from the other panel, respectively, for comparison (note the change in scale on the y axis).

eddy diffusivity are generally rapidly attenuated in the seasonal pycnocline and beyond, and their vertical profiles have well-defined responses to h_{BD} and BD. In general, stronger melt leads to higher BD, lower h_{BD}, stronger stratification N^2 in the pycnocline, larger dissipation (scaling as $\varepsilon \propto N$), and thus weaker diffusivity (scaling as $K_\rho \propto N^{-1}$) in the pycnocline. In Fig. 5, we have summarized the sensitivities of these key variables to basic hydrographic forcing. Finding the corresponding panel in the figure allows the reader to make their own inference for a given scenario of BD – h_{BD} values. For instance, we have inferred a sensitivity $\partial \log_{10} K_\rho / \partial \mathrm{BD} \approx -0.02\ (\mathrm{kg\,m^{-2}})^{-1}$.

Seasonal stratification and the associated changes in vertical mixing are key to understanding their respective contributions to and implications for the current and future state of the Arctic Ocean. Our results imply that increasing melt rates will appreciably decrease diapycnal mixing between the surface layer and the water beneath melting Arctic sea ice in summer, even further than is the case already now. In the case of solar heating, higher melt rates thus have a restoring feedback, reducing the oceanic heat flux. It is an open question whether the heat accumulated in near-surface temperature maxima is mixed up during fall (i.e., delaying the onset of freezing altogether) or only after the onset of haline convection (i.e., slowing down ice growth in winter).

The transmission and dissipation of near-inertial energy through an ice-free surface ocean and into the deep basins of the Arctic Ocean deserves further attention as it regulates ocean climate and the heat flux from Atlantic and Pacific Waters to the sea ice. Future melt rates may therefore play a crucial role in modulating ice–ocean interaction far beyond the extent of the seasonal pycnocline.

Acknowledgments. AR's work was supported through the project "CARBON BRIDGE: Bridging marine productivity regimes," a Polar Programme (project 226415) funded by the Norwegian Research Council. IF was partly supported by the Centre for Climate Dynamics at the Bjerknes Centre through Grant BASIC: Boundary Layers in the Arctic Atmosphere, Seas and Ice Dynamics. ICE-2012 and N-ICE2015 data collection was supported by the Norwegian Polar Institute's Centre for Ice, Climate and Ecosystems (ICE) through the ICE Fluxes and N-ICE2015 projects, respectively. N-ICE2015 had additional support from the Ministry of Climate and Environment and Ministry of Foreign Affairs of Norway. We thank the captains and crews of R/Vs *Helmer Hanssen* and *Lance* and all the scientists

involved in the field campaigns for their support. N-ICE2015 data are available from Norwegian Polar Data Centre (https://data.npolar.no/) under the keyword N-ICE2015. Lana Cohen provided wind and air–ice stress measurements for the N-ICE2015 campaign. Gunnar Spreen extracted and provided the sea ice concentration data for the N-ICE2015 campaign. The ice-tethered profiler data were collected and made available by the Ice-Tethered Profiler Program (Toole et al. 2011; Krishfield et al. 2008) based at the Woods Hole Oceanographic Institution (http://www.whoi.edu/itp). Two anonymous reviewers have provided valuable criticism.

REFERENCES

Anderson, R. J., 1987: Wind stress measurements over rough ice during the 1984 Marginal Ice Zone Experiment. *J. Geophys. Res.*, **92**, 6933–6941, doi:10.1029/JC092iC07p06933.

Ardyna, M., M. Babin, M. Gosselin, E. Devred, L. Rainville, and J.-E. Tremblay, 2014: Recent Arctic Ocean sea ice loss triggers novel fall phytoplankton blooms. *Geophys. Res. Lett.*, **41**, 6207–6212, doi:10.1002/2014GL061047.

Brainerd, K. E., and M. C. Gregg, 1995: Surface mixed and mixing layer depths. *Deep-Sea Res. I*, **42**, 1521–1543, doi:10.1016/0967-0637(95)00068-H.

D'Asaro, E. A., and J. H. Morison, 1992: Internal waves and mixing in the Arctic Ocean. *Deep-Sea Res.*, **39A**, S459–S484, doi:10.1016/S0198-0149(06)80016-6.

Denman, K. L., and M. Miyake, 1973: Upper layer modification at Ocean Station Papa: Observations and simulation. *J. Phys. Oceanogr.*, **3**, 185–196, doi:10.1175/1520-0485(1973)003<0185:ULMAOS>2.0.CO;2.

Dewey, R. K., and J. N. Moum, 1990: Enhancement of fronts by vertical mixing. *J. Geophys. Res.*, **95**, 9433–9445, doi:10.1029/JC095iC06p09433.

Fer, I., 2006: Scaling turbulent dissipation in an Arctic fjord. *Deep-Sea Res. II*, **53**, 77–95, doi:10.1016/j.dsr2.2006.01.003.

——, 2014: Near-inertial mixing in the central Arctic Ocean. *J. Phys. Oceanogr.*, **44**, 2031–2049, doi:10.1175/JPO-D-13-0133.1.

——, R. Skogseth, and F. Geyer, 2010: Internal waves and mixing in the Marginal Ice Zone near the Yermak Plateau. *J. Phys. Oceanogr.*, **40**, 1613–1630, doi:10.1175/2010JPO4371.1.

Gargett, A. E., and G. Holloway, 1984: Dissipation and diffusion by internal wave breaking. *J. Mar. Res.*, **42**, 15–27, doi:10.1357/002224084788506158.

Granskog, M. A., A. K. Pavlov, S. Sagan, P. Kowalczuk, A. Raczkowska, and C. A. Stedmon, 2015: Effect of sea-ice melt on inherent optical properties and vertical distribution of solar radiant heating in Arctic surface waters. *J. Geophys. Res. Oceans*, **120**, 7028–7039, doi:10.1002/2015JC011087.

——, P. Assmy, S. Gerland, G. Spreen, H. Steen, and L. Smedsrud, 2016: Arctic research on thin ice: Consequences of Arctic sea ice loss. *Eos, Trans. Amer. Geophys. Union*, **97**, doi:10.1029/2016EO044097.

Guest, P. S., and K. L. Davidson, 1987: The effect of observed ice conditions on the drag coefficient in the summer east Greenland Sea marginal ice zone. *J. Geophys. Res. Oceans*, **92**, 6943–6954, doi:10.1029/JC092iC07p06943.

Haine, T. W., and Coauthors, 2015: Arctic freshwater export: Status, mechanisms, and prospects. *Global Planet. Change*, **125**, 13–35, doi:10.1016/j.gloplacha.2014.11.013.

Hudson, S. R., M. A. Granskog, A. Sundfjord, A. Randelhoff, A. H. H. Renner, and D. V. Divine, 2013: Energy budget of first-year Arctic sea ice in advanced stages of melt. *Geophys. Res. Lett.*, **40**, 2679–2683, doi:10.1002/grl.50517.

Huisman, J., P. van Oostveen, and F. J. Weissing, 1999: Critical depth and critical turbulence: Two different mechanisms for the development of phytoplankton blooms. *Limnol. Oceanogr.*, **44**, 1781–1787, doi:10.4319/lo.1999.44.7.1781.

Itkin, P., and Coauthors, 2015: N-ICE2015 buoy data. Norwegian Polar Institute, accessed 21 Nov 2016, doi:10.21334/npolar.2015.6ed9a8ca.

Krishfield, R., J. Toole, A. Proshutinsky, and M.-L. Timmermans, 2008: Automated ice-tethered profilers for seawater observations under pack ice in all seasons. *J. Atmos. Oceanic Technol.*, **25**, 2091–2105, doi:10.1175/2008JTECHO587.1.

Levine, M. D., C. A. Paulson, and J. H. Morison, 1985: Internal waves in the Arctic Ocean: Comparison with lower-latitude observations. *J. Phys. Oceanogr.*, **15**, 800–809, doi:10.1175/1520-0485(1985)015<0800:IWITAO>2.0.CO;2.

Li, W. K. W., F. A. McLaughlin, C. Lovejoy, and E. C. Carmack, 2009: Smallest algae thrive as the Arctic Ocean freshens. *Science*, **326**, 539, doi:10.1126/science.1179798.

Lincoln, B. J., T. P. Rippeth, Y.-D. Lenn, M. L. Timmermans, W. J. Williams, and S. Bacon, 2016: Wind-driven mixing at intermediate depths in an ice-free Arctic Ocean. *Geophys. Res. Lett.*, **43**, 9749–9756, doi:10.1002/2016GL070454.

Martin, T., M. Steele, and J. Zhang, 2014: Seasonality and long-term trend of Arctic Ocean surface stress in a model. *J. Geophys. Res. Oceans*, **119**, 1723–1738, doi:10.1002/2013JC009425.

McPhee, M. G., and L. H. Kantha, 1989: Generation of internal waves by sea ice. *J. Geophys. Res.*, **94**, 3287–3302, doi:10.1029/JC094iC03p03287.

——, G. A. Maykut, and J. H. Morison, 1987: Dynamics and thermodynamics of the ice/upper ocean system in the marginal ice zone of the Greenland Sea. *J. Geophys. Res.*, **92**, 7017–7031, doi:10.1029/JC092iC07p07017.

——, T. P. Stanton, J. H. Morison, and D. G. Martinson, 1998: Freshening of the upper ocean in the Arctic: Is perennial sea ice disappearing? *Geophys. Res. Lett.*, **25**, 1729–1732, doi:10.1029/98GL00933.

Morison, J., C. E. Long, and M. D. Levine, 1985: Internal wave dissipation under sea ice. *J. Geophys. Res.*, **90**, 11 959–11 966, doi:10.1029/JC090iC06p11959.

——, R. Kwok, C. Peralta-Ferriz, M. Alkire, I. Rigor, R. Andersen, and M. Steele, 2012: Changing Arctic Ocean freshwater pathways. *Nature*, **481**, 66–70, doi:10.1038/nature10705.

Moum, J. N., 1996: Energy-containing scales of turbulence in the ocean thermocline. *J. Geophys. Res.*, **101**, 14 095–14 109, doi:10.1029/96JC00507.

Osborn, T. R., 1980: Estimates of the local rate of vertical diffusion from dissipation measurements. *J. Phys. Oceanogr.*, **10**, 83–89, doi:10.1175/1520-0485(1980)010<0083:EOTLRO>2.0.CO;2.

Peralta-Ferriz, C., and R. A. Woodgate, 2015: Seasonal and interannual variability of pan-Arctic surface mixed layer properties from 1979 to 2012 from hydrographic data, and the dominance of stratification for multiyear mixed layer depth shoaling. *Prog. Oceanogr.*, **134**, 19–53, doi:10.1016/j.pocean.2014.12.005.

Peterson, A. K., I. Fer, M. G. McPhee, and A. Randelhoff, 2017: Turbulent heat and momentum fluxes in the upper ocean under Arctic sea ice. *J. Geophys. Res. Oceans*, **122**, 1439–1456, doi:10.1002/2016JC012283.

Proshutinsky, A., and Coauthors, 2009: Beaufort Gyre freshwater reservoir: State and variability from observations. *J. Geophys. Res.*, **114**, C00A10, doi:10.1029/2008JC005104.

Randelhoff, A., A. Sundfjord, and A. H. H. Renner, 2014: Effects of a shallow pycnocline and surface meltwater on sea ice–ocean drag and turbulent heat flux. *J. Phys. Oceanogr.*, **44**, 2176–2190, doi:10.1175/JPO-D-13-0231.1.

——, I. Fer, A. Sundfjord, J.-E. Tremblay, and M. Reigstad, 2016: Vertical fluxes of nitrate in the seasonal nitracline of the Atlantic sector of the Arctic Ocean. *J. Geophys. Res. Oceans*, **121**, 5282–5295, doi:10.1002/2016JC011779.

Rudels, B., 2016: Arctic Ocean stability: The effects of local cooling, oceanic heat transport, freshwater input, and sea ice melt with special emphasis on the Nansen Basin. *J. Geophys. Res. Oceans*, **121**, 4450–4473, doi:10.1002/2015JC011045.

——, E. P. Jones, U. Schauer, and P. Eriksson, 2004: Atlantic sources of the Arctic Ocean surface and halocline waters. *Polar Res.*, **23**, 181–208, doi:10.3402/polar.v23i2.6278.

Spreen, G., L. Kaleschke, and G. Heygster, 2008: Sea ice remote sensing using AMSR-E 89-GHz channels. *J. Geophys. Res.*, **113**, C02S03, doi:10.1029/2005JC003384.

Stein, R., and R. W. MacDonald, Eds., 2004: *The Organic Carbon Cycle in the Arctic Ocean*. Springer-Verlag, 363 pp.

Stroeve, J. C., M. C. Serreze, M. M. Holland, J. E. Kay, J. Malanik, and A. P. Barrett, 2012: The Arctic's rapidly shrinking sea ice cover: A research synthesis. *Climatic Change*, **110**, 1005–1027, doi:10.1007/s10584-011-0101-1.

Sundfjord, A., I. Fer, Y. Kasajima, and H. Svendsen, 2007: Observations of turbulent mixing and hydrography in the marginal ice zone of the Barents Sea. *J. Geophys. Res. Oceans*, **112**, C05008, doi:10.1029/2006JC003524.

Timmermans, M.-L., and P. Winsor, 2013: Scales of horizontal density structure in the Chukchi Sea surface layer. *Cont. Shelf Res.*, **52**, 39–45, doi:10.1016/j.csr.2012.10.015.

——, A. Proshutinsky, R. A. Krishfield, D. K. Perovich, J. A. Richter-Menge, T. P. Stanton, and J. M. Toole, 2011: Surface freshening in the Arctic Oceans Eurasian Basin: An apparent consequence of recent change in the wind-driven circulation. *J. Geophys. Res.*, **116**, C00D03, doi:10.1029/2011JC006975.

——, S. Cole, and J. Toole, 2012: Horizontal density structure and restratification of the Arctic Ocean surface layer. *J. Phys. Oceanogr.*, **42**, 659–668, doi:10.1175/JPO-D-11-0125.1.

Toole, J., R. Krishfield, M.-L. Timmermans, and A. Proshutinsky, 2011: The ice-tethered profiler: Argo of the Arctic. *Oceanography*, **24**, 126–135, doi:10.5670/oceanog.2011.64.

Yamazaki, H., and T. Osborn, 1990: Dissipation estimates for stratified turbulence. *J. Geophys. Res.*, **95**, 9739–9744, doi:10.1029/JC095iC06p09739.